NANO · MICRO small
www.small-journal.com

Robust Amide-Linked Fluorinated Covalent Organic Framework for Long-Term Oxygen Reduction Reaction Electrocatalysis

Miguel Jiménez-Duro, Emiliano Martínez-Periñán, Marcos Martínez-Fernández, José I. Martínez, Encarnación Lorenzo, and José L. Segura**

The high energy demand of the evolving world opens the door to develop more sustainable and environmentally friendly energy sources. Oxygen reduction reaction (ORR) is a promising candidate, being the $2e^-$ pathway of great interest for the green production of hydrogen peroxide. Metal-free covalent organic frameworks (COFs) electrocatalysts present a suitable alternative to substitute the noble-metals more commonly employed in this application. However, the lability of the linkages building up the framework raises an issue for their long-term use and application in aggressive media. Herein, a stable amide-linked COF is reported through post-synthetic modification of a previously reported imine-linked COF proven to be effective as an electrocatalyst, enhancing its chemical stability and electrochemical response. It is found that after the linkage transformation, the new electrocatalyst displays a higher selectivity toward the H_2O_2 production (98.5%) and an enhanced turnover frequency of 0.155 s^{-1}, which is among the bests reported to date for metal-free and COF based electrocatalysts. The results represent a promising step forward for metal-free non pyrolyzed electrocatalysts, improving their properties through post-synthetic linkage modification for long-term operation.

1. Introduction

In recent decades, the demand for sustainable energy and manufacture has increased, primarily due to the depletion of fossil fuel reserves and the resulting environmental pollution.[1] To address this challenge, the development of new and more sustainable energy sources is imperative. One promising candidate is the production of electrical energy from the chemical energy of abundant and environmentally friendly compounds.[2–4] In this field, the oxygen reduction reaction (ORR) is highly efficient and is found in nature. However, this process exhibits low kinetics,[5] necessitating the assistance of catalysts to accelerate the reaction kinetics. These catalysts are categorized based on the selectivity of the process: (i) a 4-electron pathway reduction of O_2 to H_2O, which is relevant for energy-related applications such as metal-air batteries, and (ii) the 2-electron pathway reduction of O_2 to H_2O_2 which is significant for the clean and in situ production of hydrogen peroxide. As for the two-electron pathway, the elimination of storage and transportation costs makes this redox reaction a viable option for the environmentally friendly production of hydrogen peroxide, which is in high demand in many industries such as the chemical and medical sectors.[6,7] Even though noble-metal catalysts are the most widely used,[8,9] their high cost and limited reserves hinder their commercial

M. Jiménez-Duro, M. Martínez-Fernández, J. L. Segura
Facultad de CC. Químicas
Universidad Complutense de Madrid
Avenida Complutense s/n, Madrid 28040, Spain
E-mail: segura@ucm.es

E. Martínez-Periñán, E. Lorenzo
Departamento de Química Analítica y Análisis Instrumental
Facultad de Ciencias
Universidad Autónoma de Madrid
Campus de Cantoblanco–Crta. Colmenar, Madrid 28049, Spain
E-mail: encarnacion.lorenzo@uam.es

E. Martínez-Periñán, E. Lorenzo
Institute for Advanced Research in Chemical Sciences (IAdChem)
Universidad Autónoma de Madrid Campus de Cantoblanco
Madrid 28049, Spain

J. I. Martínez
Departamento de Nanoestructuras, Superficies, Recubrimientos y Astrofísica Molecular
Instituto de Ciencia de Materiales de Madrid (ICMM-CSIC)
Madrid 28049, Spain

E. Lorenzo
Instituto Madrileño de Estudios Avanzados en Nanociencia (IMDEA-Nanociencia) Cantoblanco
Madrid 28049, Spain

The ORCID identification number(s) for the author(s) of this article can be found under https://doi.org/10.1002/smll.202402082

DOI: 10.1002/smll.202402082

applications.[10] An interesting approach to address this problem is the development of metal-free electrocatalysts[11] to overcome these challenges, and non-pyrolyzed covalent organic frameworks present a promising alternative for the development of highly selective catalysts.[12]

Covalent organic frameworks (COFs) are a type of porous and crystalline materials first described in 2005.[13] Their excellent properties, such as porosity, crystallinity, pre-designability and stability,[14,15] among others, make them great candidates for applications in diverse fields as gas adsorption,[16] batteries,[17] water harvesting,[18] sensors[19] and more. Previous studies have reported COFs as highly effective and selective metal-free/non-pyrolyzed catalyst for both the 4-electron[20–22] and for the 2-electron pathways,[23–25] which are of interest for studying structural-property relationships in order to improve the electrocatalytic performance of novel materials. COFs are formed through the union of molecular-building blocks (linkers) by covalent bonds (linkages). The most common reaction employed is the Schiff-base condensation to yield imine-linked COFs,[26] due to its high reversibility/stability ratio and the wide availability of aromatic amines and aldehydes for synthesis.[27] Consequently, most metal-free and non-pyrolyzed COF-based electrocatalysts are constructed using this specific reaction. However, the imine-linkage still exhibits some lability, especially in acidic and basic media,[28] which are the typical media provided by the supporting electrolytes for the ORR process.[29] For this reason we hypothesize that post-synthetic modification of the imine bond to more robust amide linkages could improve the stability of the ORR process and increase the lifetime of the catalyst employed.[30]

In this work, we report the post-synthetic modification of an imine-bonded fluorinated COF (**Imine-F-COF**)[23] by the chemical oxidation of the imine linkages mediated with $NaClO_2$, yielding a more stable-amide bonded framework (**Amide-F-COF**). The post-synthetic transformation was rationally studied, demonstrating that the incorporation of amide functionalities into the highly fluorinated COF enhances the robustness of the framework and its electrocatalytic properties. Finally, the adsorption of the ORR intermediates was examined using DFT calculations, revealing the most probable adsorption carbon-site and the mechanism.

2. Results and Discussion

2.1. Synthesis and Characterization

Imine F-COF was synthesized by the Schiff base reaction between 1,3,5-tris(2,3,5,6-tetrafluoroaniline)-benzene (**DFTAPB**) and 2,3,4,6-tetrafluoroterepthaldehyde (**TFTA**) at room temperature in THF/TFA following a previously reported procedure.[23] The post-synthetic oxidation of **Imine-F** was carried out using $NaClO_2$ as an oxidant and 2-methyl-2-butene in Dioxane/AcOH at room temperature for 2 days,[31] resulting in the formation of **Amide F-COF** as a white powder (see ESI for more details).(**Scheme 1**)

The successful transformation of the imine-linkages to the amide bonds was monitored by Fourier transform infrared (FTIR) spectroscopy and ^{13}C cross-polarization magic angle spinning nuclear magnetic resonance (^{13}C-CP-MAS-NMR). On one hand, the FTIR spectra (**Figure 1A**; Figure S1, Supporting Information) showed the fading of the imine N = C stretching at 1622 cm^{-1} accompanied by the emergence of two amide C = O absorption bands at 1702 cm^{-1} and at 1652 cm^{-1}, corresponding to the free carbonyls and associated aromatic amide functionalities via interlayer hydrogen-bonds.[32] This was corroborated with the appearance of two new sorption bands at 3425 cm^{-1} and 3250 cm^{-1} corresponding to the free and associated N-H stretchings, respectively. In addition, the C-F stretching at 1315, 990, and 673 cm^{-1} were retained, confirming that the fluorinated skeleton remains intact after the oxidation of the linkages.[33] On the other hand, the ^{13}C-CP-MAS-NMR of the obtained powders (Figure 1B; Figures S2 and S3, Supporting Information) revealed the chemical transformation by observing the amide linkages, which appear downfield (≈160 ppm) with respect to the anisochronous carbons of the imine (≈158 ppm).[31,34–38] Furthermore, the signals corresponding to the aromatic backbone remained around 150–110 ppm, confirming the selectivity of the chemical process at the atomic scale.

The porous features were investigated through nitrogen sorption isotherms at 77 K (Figure 1C; Figures S4 and S5, Supporting Information), revealing type IV isotherms for both materials, indicating mesoporous nature. From this data, the Brunauer-Emmet-Teller (BET) areas were obtained, being 1270 and 286 $m^2\ g^{-1}$ for imine-linked and amide-linked COFs, respectively. The pore volumes decreased from 1.24 $cm^3\ g^{-1}$ to 0.233 $cm^3\ g^{-1}$ with the post-synthetic treatment. It is worth mentioning that the post-synthetic modification of COFs often lead to partial "amorphization" of some domains within the frameworks due to the exchange of the Csp2 to Csp3 during the reaction the amide formation. Consequently, while some pores remain crystalline, other regions of the network collapse, decreasing its crystallinity.[31,34,35,37,38] Finally, the pore size distributions calculated by the non-local density functional theory (NLDFT) was also reduced, being mainly centered at 30 Å and at 27.5 Å for the imine-linked (Figure S8, Supporting Information) and amide-linked (Figure S9, Supporting Information) COFs, respectively.

The crystalline nature of the obtained polymers was evidenced through powder X-ray diffraction (PXRD). Thus, both materials present similar diffraction patterns (Figure 1D; Figures S10 and S11, Supporting Information), revealing that the periodicity of the network remains unaltered after the post-synthetic modification. Interestingly, the diffraction maxima corresponding to the **Amide F-COF** appears shifted toward larger 2theta values compared to those of the bare **Imine F-COF**. Thus, the diffraction maxima at 2.65°, 4.68°, 5.43°, 7.23°, 9.51°, 9.88° and 24.36° correspond to the imine-linked material, while those recorded at 2.83°, 4.91°, 5.63°, 7.39°, 9.69°, 10.09° and 24.71° correspond to the amide-based COF. Additionally, an analysis of the full-with at medium height (FWMH) of the (100) diffraction was employed to estimate the degree of crystallinity of the materials, confirming the retention of the crystalline nature of the network after the post-synthetic modification. Excellent FWMH values of 0.327° and 0.373° were obtained for **Imine F-COF** and **Amide F-COF**, respectively.[39]

Finally, the results of the simulations yield both 2D structures with canonical hexagonal P6 symmetry, featuring lattice parameters $a = b = 37.49$ for the **Imine F-COF** and $a = b = 37.81$ Å for **Amide F-COF**. Both structures exhibit preferential eclipsed (AA) stacking configurations, typically consistent with $\pi-\pi$ stacking

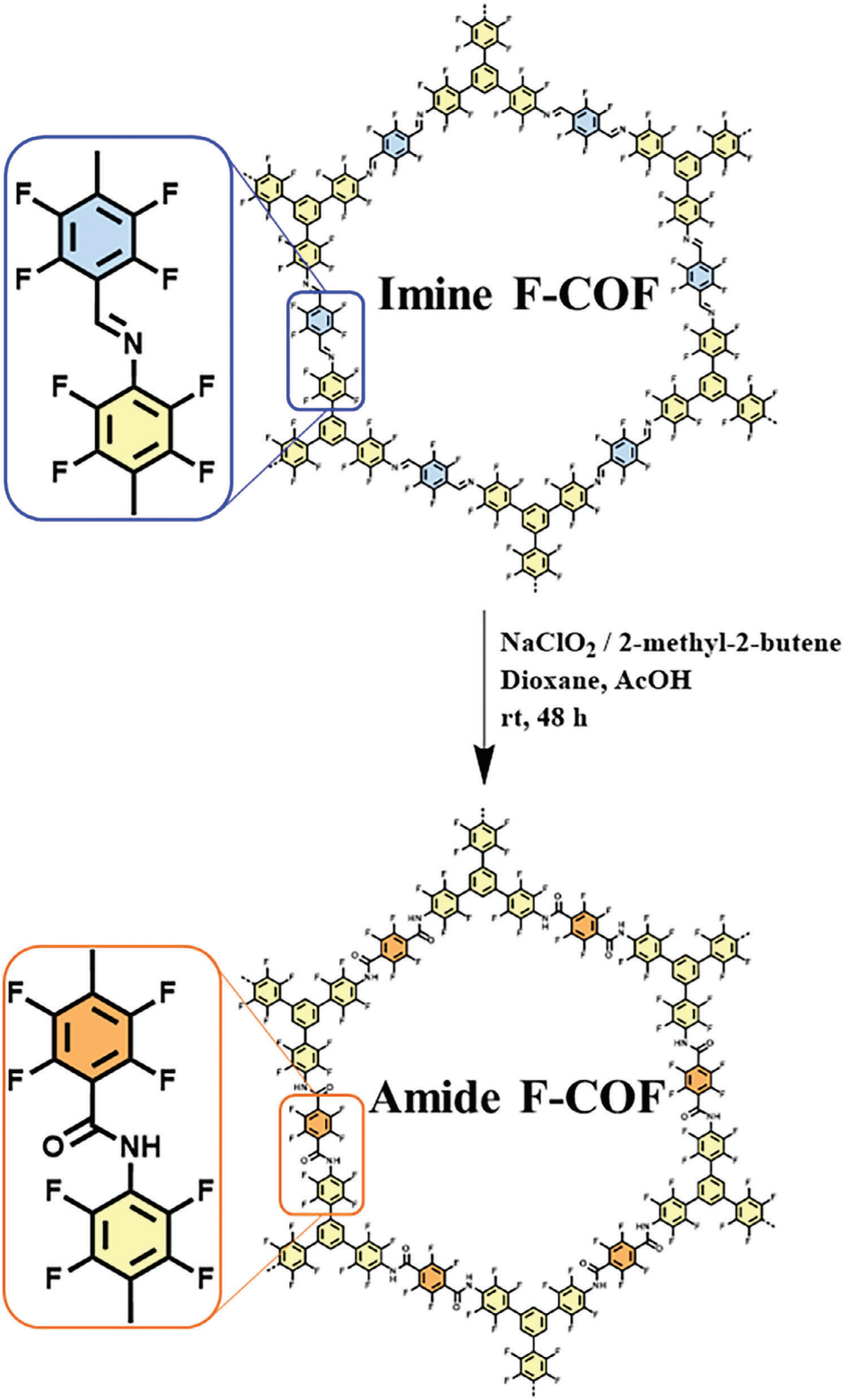

Scheme 1. Synthesis of Amide F-COF.

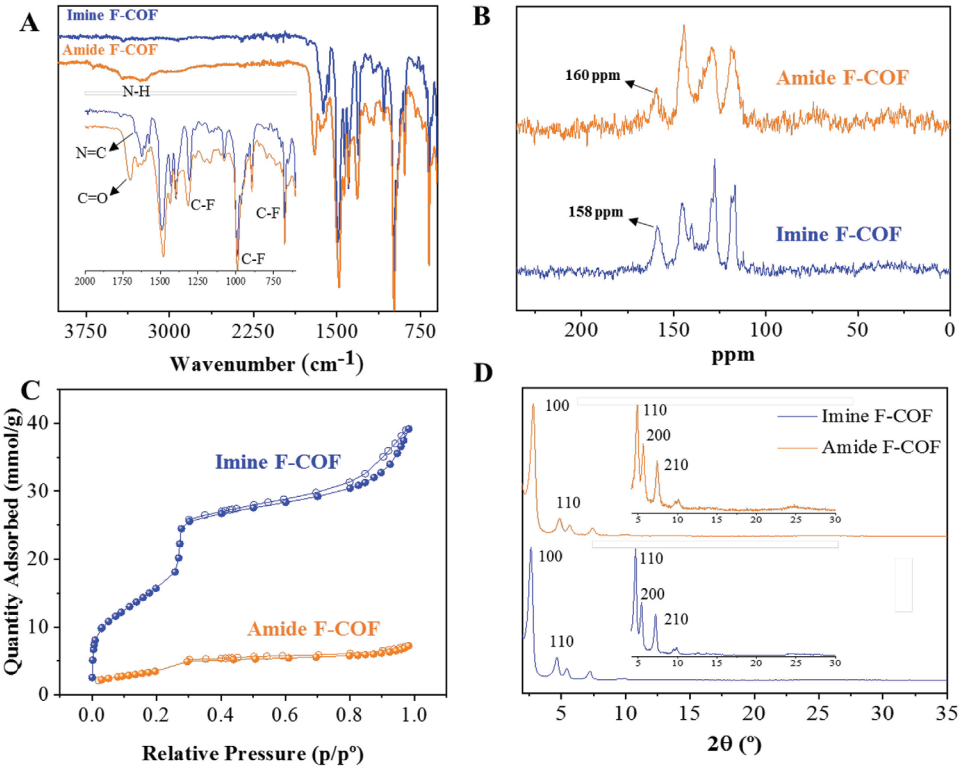

Figure 1. A) FTIR spectra. B) ^{13}C CP/MAS-NMR spectra. C) Nitrogen sorption isotherms at 77 K. D) PXRD patterns. The inset shows a magnification in the 4–30° range.

interlayer distances of $c = 3.63$ (**Imine F-COF**) and 3.89 Å (**Amide F-COF**) as shown in **Figure** 2A. In the case of the **Amide F-COF**, it is noteworthy to highlight a slight layer displacement due to an interlayer hydrogen bond between the amide linkages, which aligns well with observations from FTIR and pore size distributions (*vide supra*). We simulated the corresponding diffractograms based on these optimized structures (Figure 2B; Figures S12 and S13, Supporting Information), which show excellent agreement with the experimental evidence, thus reinforcing the validity of the structures derived from simultaneous structure + cell DFT geometrical optimizations. Furthermore, the results obtained were corroborated by performing Pawley refinement by using GSAS-II[40] demonstrating good correlations with the lattice parameters a = b = 37.38 Å; c = 3.57 Å for **Imine F-COF** (Rw = 14.767; $\chi 2 = 14.767$) and $a = b = 37.75$ Å; $c =$ 3.70 Å for **Amide F-COF** (Rw = 11.416; $\chi 2 = 4.66$) as shown in Figure S14 (Supporting Information).

The morphology of the materials was investigated through scanning electron microscopy (SEM), revealing that the polygranular composition is maintained after the post-synthetic transformation (Figure 3; Figures S15 and S16, Supporting Information). Furthermore, energy dispersive X-ray spectroscopy (EDX) was carried out to further study the elemental composition of the material (Figure S17, Supporting Information) ensuring no impurities of $NaClO_2$ remain from the oxidation process. Moreover, we studied the suspension of the materials in a H_2O/Ethanol (7/3) mixture (0.4 mg mL^{-1}) with an ultrasonic bath (35 kHz, 80 W) and their subsequent drop-casting, as this protocol is widely used for modifying glassy-carbon electrodes. The colloidal nature of the materials was observed by the Tyndall effect. Additionally, dynamic light scattering (DLS) showed a decrease in the hydrodynamic sizes of the particles, with monomodal distributions around 716 ± 5 nm for **Imine F-COF** and 595 ± 12 nm for **Amide F-COF** (Figure S25–S27, Supporting Information). Finally, transmission electron microscopy (TEM) of the drop-casted materials revealed that the particle size and morphology remain unaltered after the ultrasonication process, maintaining the rod-like fibers with sizes around 80 nm that composes the agglomerates (**Figure 3**; Figures S15 and S16, Supporting Information). TEM-FTT was performed using ImageJ software to analyze the observed spaces obtaining values of 1.83 nm for **Imine F-COF** (Figure S18, Supporting Information) and 1.81 nm for **Amide F-COF** (Figure S19, Supporting Information), which corresponds to the (110) facers appearing at 4.8359 and 4.8879 of 2theta values, respectively (being 1.827 and 1.808 nm the Bragg's law transformed distances). It should be highlighted that the variation of the catalyst size is an important factor to consider when comparing materials, as an increase in particle-size could potentially decrease the overall-electrocatalytic performance and even the selectivity of the process.[41,42]

To gain insights into the stability of both frameworks, thermogravimetric analysis (TGA) under a nitrogen atmosphere was conducted to study thermal stability, while for chemical stability, both COFs were suspended in highly corrosive environments. On one hand, thermal stability is retained after the post-synthetic transformation. Thus, while degradation of

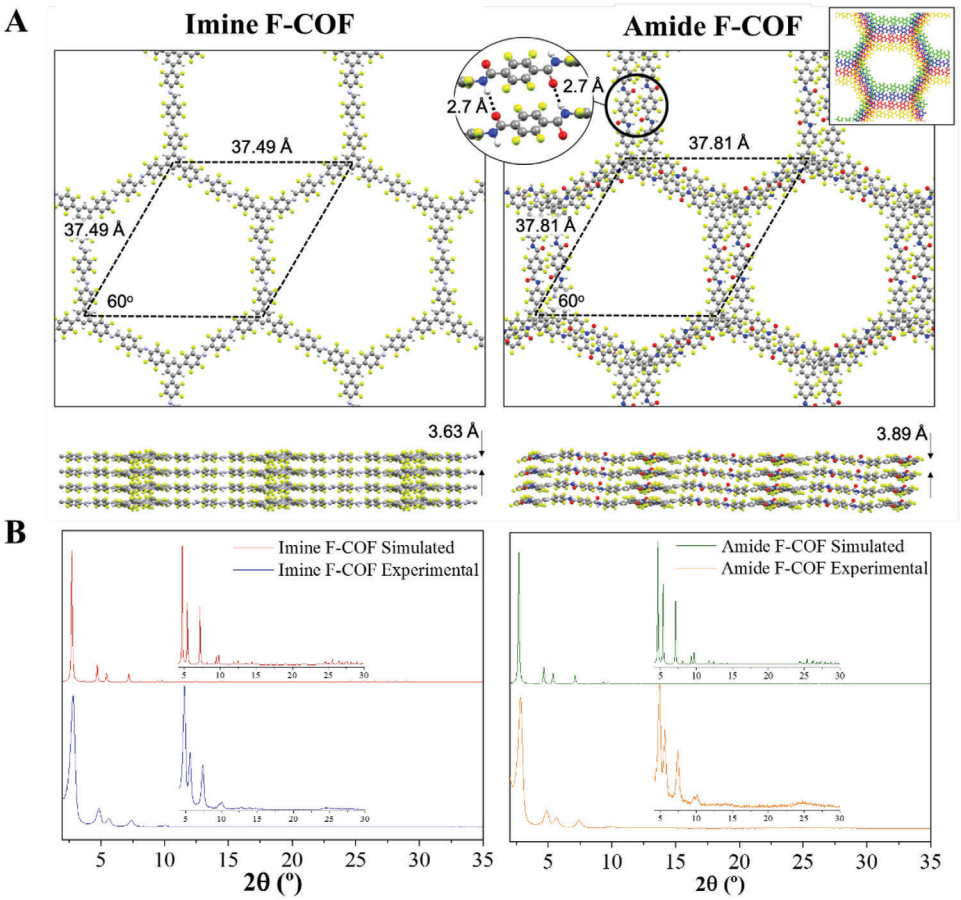

Figure 2. A) Top and side pictorial views of the DFT-optimized structures for the Imine F-COF (left) and Amide F-COF (right) crystal bulks, indicating the resulting computed unit cells and interlayer distances, both with the preferential AA eclipsed interlayer stacking configuration. B) Experimental and simulated diffractograms obtained from the resulting DFT-optimized structures the Imine F-COF (left) and Amide F-COF (right).

Amide-F-COF starts at 427 °C (Figure S21, Supporting Information), degradation of **Imine-F-COF** (Figure S20, Supporting Information) starts at 450 °C. To further investigate the thermal stability, both COFs were placed in vacuum-sealed ampoules and thermally treated at 300 °C for 16 h. PXRD was utilized to analyze potential amorphization of the frameworks The obtained diffractograms demonmstrate the retention of the crystalline features for both frameworks, consistent with the findings of Dichtel et al. (Figures S22 and S23, Supporting Information).[43] On the other hand, chemical stability is greatly increased for **Amide F-COF**, as demonstrated by the following tests conducted in HCl 12 M and KOH 12 M solutions, where 8 mg of each COF is suspended in 1 mL of each solution at 30 °C for 24 h. The powders were then recovered by filtration and washed with water, THF and hexane several times. After treatment of the powders, **Imine F-COF** was completely dissolved, while **Amide F-COF** remained as a white solid, recovering around 83% of the original mass. PXRD was employed to analyze the retainment of the crystalline features, observing four prominent maxima after exposure to HCl 12 M indicating great resistance to the acid medium. Meanwhile, after exposure to NaOH 12 M only the (100) diffraction was observed with an obvious increase of the FWMH value, indicating less resistance to the base medium (Figure S24, Supporting Information).

Finally, ultraviolet-visible by diffuse reflectance (DR-UV–vis) spectroscopy measurements were carried out to study the optical bandgap of both COFs (Figure S28, Supporting Information). As shown in Figures S29 and S30 (Supporting Information), the optical band gap increased from 2.64 eV for **Imine F-COF** to 2.81 eV for **Amide F-COF** due to the loss of conjugation, explaining the loss of color after the post-synthetic modification. Furthermore, the computed band structure for the **Imine F-COF** and **Amide F-COF** crystal bulks (**Figure 4**) follows the *k*-path Γ→K→M→Γ connecting the most representative symmetry points.

Both compounds are theoretically predicted as narrow-gap semiconductors, with resulting band gaps of 1.63 and 2.03 eV for the **Imine F-COF** and **Amide F-COF**, respectively, and show a very poor band dispersion for the band-states closest to the Fermi energy. 3D isosurfaces corresponding to the valence (VB) and conduction (CB) for the F-COF amide system are also shown in Figure 4. Valence bands are basically located in the 1,3,5-tris(2,3,5,6-tetrafluoro)-benzene unit, whilst the conduction band seems to be preferentially located in the 2,3,4,6-tetrafluoroterepthaldehyde-derived unit.

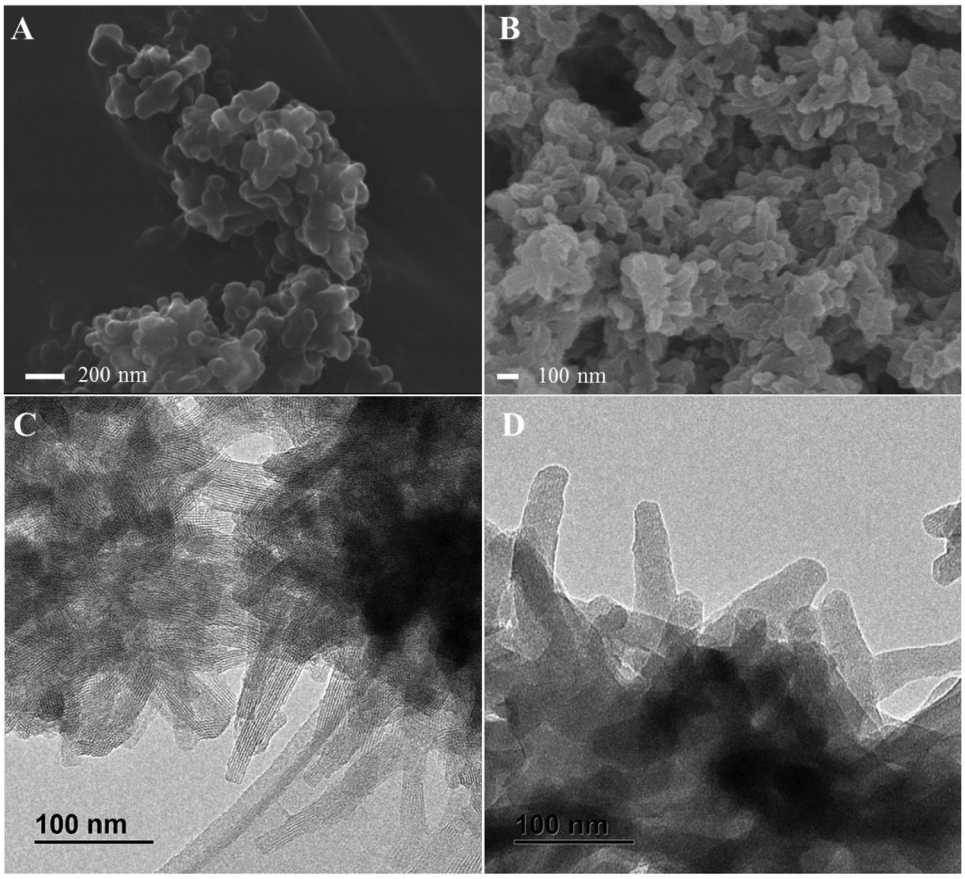

Figure 3. A) SEM micrograph of Imine F-COF with a scale of 200 nm. B) SEM micrograph of Amide F-COF with a scale of 100 nm. C) TEM micrograph of Imine F-COF with a scale of 100 nm. D) TEM micrograph of Amide F-COF with a scale of 100 nm.

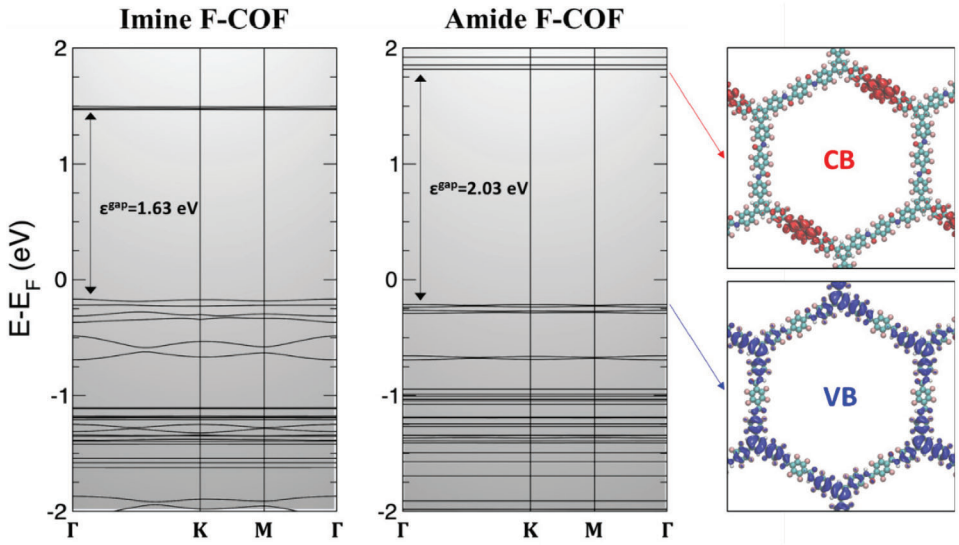

Figure 4. Calculated band structure for Imine F-COF and Amide F-COF crystal bulks. Band gap is indicated for each case. 3D isosurfaces corresponding to the valence (VB) and conduction (CB) are shown for the Amide F-COF system.

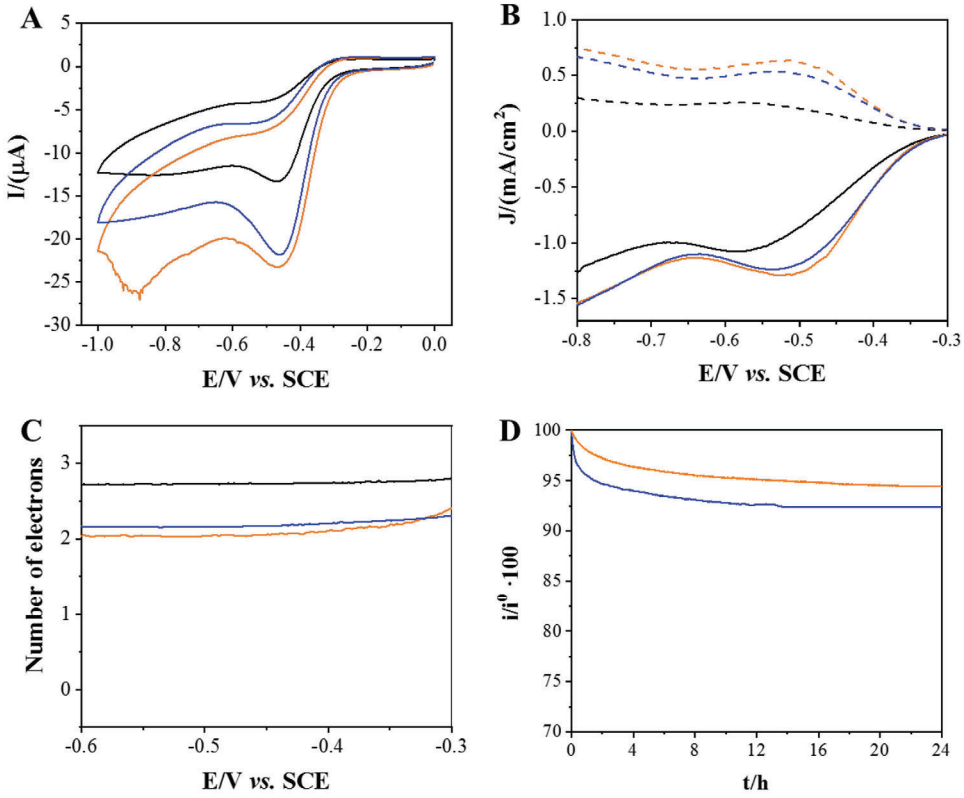

Figure 5. A) Cyclic voltammograms recorded in static regimen in O_2 saturated 0.1 M KOH at 10 mV s^{-1}. B) HLSV recorded using Pt ring/modified GC disc electrode in O_2 saturated 0.1 M KOH at 10 mV s^{-1} applying 1000 RPM (continuous line disc current and dash line ring current). C) Number of electrons involved in ORR calculated from data in B. D) Current stability applying −0.4 V versus SCE. Black is the bare GC electrode; blue is Imide F-COF/GC and orange is Amide F-COF/GC.

2.2. Electrochemical Measurements

Cyclic voltammograms at glassy carbon (GC) electrodes modified with **Imine F-COF** (**Imine F-COF**/GC) or **Amide F-COF** (**Amide F-COF**/GC) in the absence of oxygen do not show redox peaks (Figure S31, Supporting Information), which agrees with the absence of electroactive moieties in the COFs structures. In a saturated oxygen 0.1 M KOH solution (**Figure 5A**), **Imine F-COF**/GC, **Amide F-COF**/GC and bare GC electrodes showed electrocatalytic activity through oxygen reduction. In the case of **Imine F-COF**/GC, the oxygen reduction peak showed an onset potential of around 25 mV before the onset for ORR of GC electrode and in the case of **Amide F-COF**/GC the onset potential decrease is around 42 mV. The current intensity also increases significantly when **Imine F-COF**/GC and **Amide F-COF**/GC are employed compared with bare GC, being the current increase a bit higher in the case of **Amide F-COF**/GC. Electrochemical impedance spectroscopy (EIS) results, as can be observed in the Nyquist plot (Figure S32, Supporting Information), agree with the results described above, showing a significant decrease of the charge transfer for ORR when **Imine F-COF**/GC and **Amide F-COF**/GC are employed, being higher in the case of **Amide F-COF**/GC. Tafel slopes obtained from CVs are showed at Figure S33 (Supporting Information). As can be observed, the Tafel slope decreases when comparing **Imine F-COF**/GC and **Amide F-COF**/GC with the GC electrode, with the slope being lower in the case of **Amide F-COF**/GC. This suggests a better disposition of the **Amide F-COF** material for ORR electrocatalysis. To elucidate the conductivity of COFs, EIS experiments using $(Fe(CN)_6^{4-}/Fe(CN)_6^{3-})$ as a redox probe were conducted. The Nyquist plot (Figure S34, Supporting Information) demonstrated that when COF materials are deposited onto the GC electrode (**Imine F-COF**/GC and **Amide F-COF**/GC), as expected, the non-conductive behavior of COF compounds increases the resistance to electron transfer of the redox probe.

Hydrodynamic linear sweep voltammetry (HLSV) using a rotating Pt/CG ring-disc electrode was employed to study the electrocatalytic behavior of the COFs materials towards ORR (Figure 5B). The potential of the modified working electrode was varied in order to oxidize and detect the H_2O_2 generated during the ORR, while in the case of the platinum ring it was set at +0.25 V versus SCE. As expected, HLSV showed a decrease in the onset potential for ORR and an increase in the cathodic current for **Imine F-COF**/GC and **Amide F-COF**/GC modified electrodes compared to bare GC, indicating that both COF materials show an improved electrocatalytic behavior to ORR, being better for the **Amide F-COF**/GC electrode, as inferred from the lower overpotential for ORR and the higher current recorded. When the **Amide F-COF**/GC electrode is used, the Pt ring current is also higher, indicating a greater amount of H_2O_2 being produced, which implies a higher H_2O_2 yield. Calculation of H_2O_2 yields showed that **Amide F-COF**/GC (98.5%) outperforms the reported

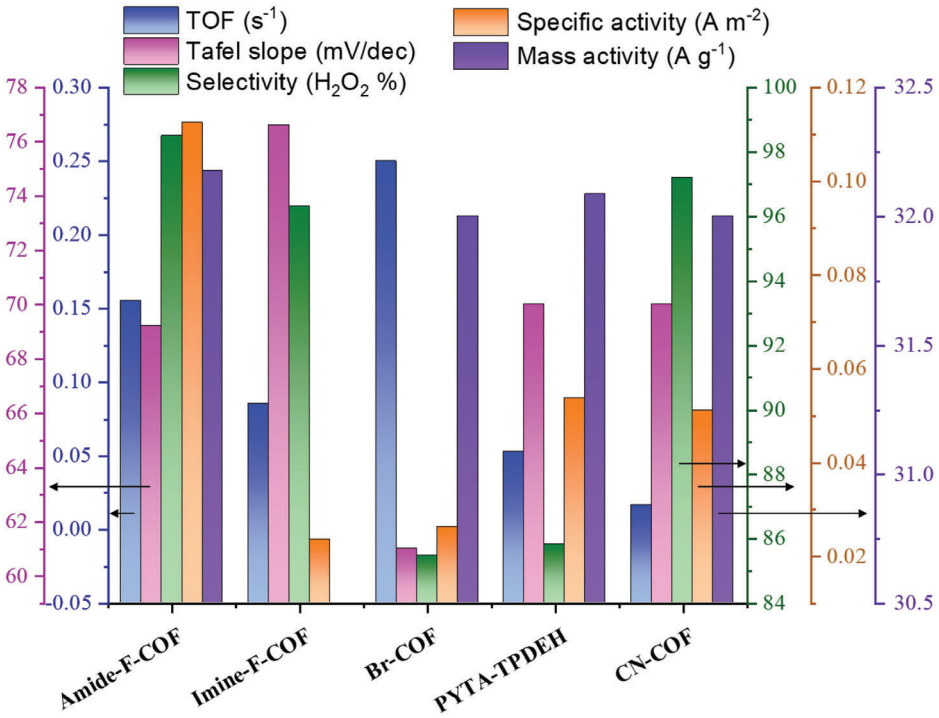

Figure 6. TOF, mass activity, H_2O_2 selectivity and specific activity comparison between Imine F-COF and Amide F-COF with other reported metal-free and non-pyrolized COFs.[23–25,44]

values for **Imine F-COF**/GC (96.3%) and is significantly superior compared to GC (78.9%). The faradaic efficiency (FE_{RRDE}) also demonstrated the superior capacity for H_2O_2 production using **Amide F-COF**/GC (97.1%) compared to the reported values for **Imine F-COF**/GC (71.1%) and GC (58.1%). These excellent properties for H_2O_2 production can be explained by examining the number of electrons exchanged during ORR (Figure 5C). The **Amide F-COF**/GC electrode exchange 2.02 electrons, a value that is very close to the theoretical 2-electron mechanism of O_2 reduction into H_2O_2. This value is even closer to 2 than the previously reported for **Imine F-COF**/GC (2.10 electrons), indicating a higher selectivity for the 2-electron ORR mechanism compared to the 4-electron mechanism. Regarding the stability of both ORR electrocatalysts (**Imine F-COF**/GC and **Amide F-COF**/GC), both showed extraordinary results, as is observed in Figure 5D, maintaining a high percentage of their initial current, 94.5% and

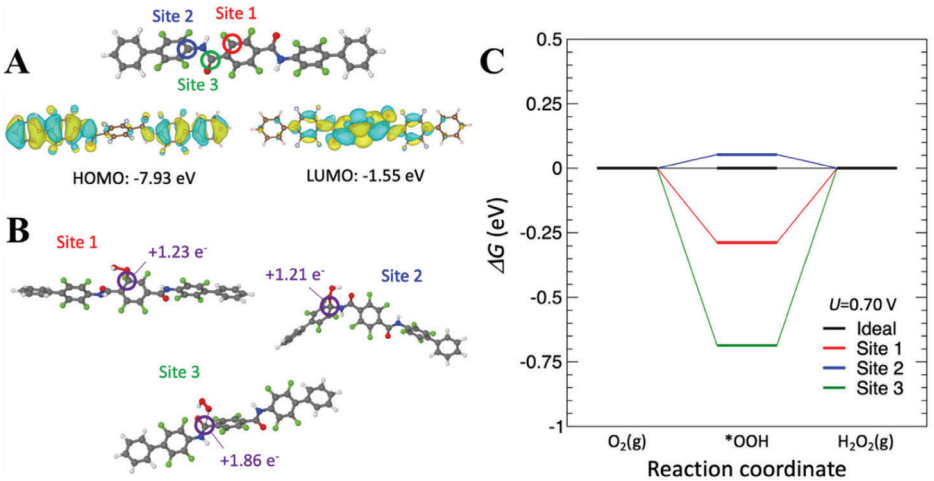

Figure 7. A) DFT-optimized geometry corresponding to the Amide F-COF representative fragment model to evaluate the $2e^-$-ORR, indicating the active sites. HOMO and LUMO values and 3D-isosurfaces are also shown in the panel. B) DFT-optimized geometries corresponding to the key *OOH intermediates adsorbed on the active sites of the Amide F-COF fragment mode and the calculated Bader charges. C) Computed free energy reaction profiles for the $2e^-$-ORR processes mediated by the Amide F-COF at the three different active site and electrode potential of 0.70 V.

92.4% respectively, after 24 hours of operation keeping the potential at 0.5 V versus SCE. Also, good stability during successive LSV scans (Figures S35 and S36, Supporting Information) were obtained, keeping constant the density current values of modified Imine F-COF/GC and Amide F-COF/GC disc electrodes and their corresponding Pt ring density current, which is clear evidence of the stability during hydrogen peroxide production rate

(TabTo compare the products with other reported metal-free and non-pyrolyzed COF-based electrocatalysts, we employed parameters such as turnover frequency (TOF), Tafel slopes, H_2O_2 selectivity, mass activity and specific activity (**Figure 6**). First, TOF was calculated at 0.5 V versus RHE (see ESI for more details). As expected, **Amide F-COF**/GC shows a higher TOF value of 0.155 s^{-1} than **Imine F-COF**/GC (0.085 s^{-1}), which is significantly high compared to other metal-free and non-pyrolyzed COF materials used as ORR electrocatalyst in the literature. **Amide F-COF** exhibits the second lowest Tafel slope and the second highest TOF among of the reported COFs. While Br-COF yields the highest TOF, it shows less selectivity toward the 2-electron mechanism and H_2O_2 production (Figure 6)[44] than **Amide F-COF** and it has stability disadvantages due to the more labile nature of the imine-linkage. Finally, **Amide F-COF** displays an excellent specific activity value (0.1125 mA×m^{-2}) which is ten times higher than for the rest of the catalysts reported to date, while the mass activity (32.17 A×g^{-1}) falls in the same range. (Table 1)

To further study **Amide F-COF** as an ORR electrocatalyst, we have computationally investigated the 2e-$^-$ORR process mediated by the fragment model shown in **Figure** 7A, as representative of the **Amide F-COF**. The adoption of this simplistic and reductionist model to compute the 2e$^-$-ORR catalysis is justified by the successful results obtained for the similar system recently reported,[23] and by the morphological and electronic consistency between the HOMO and LUMO isosurfaces of Figure 7A, and those corresponding to the valence and conduction bands of Figure 4.

This 2e$^-$-ORR mechanism involves two elemental steps: i) first, O_2 is reduced to an adsorbed *OOH intermediate, and ii) a subsequent reduction of the *OOH leads to the H_2O_2 release. The electrode applied potential has been selected as the equilibrium potential of the O_2 reduction to H_2O_2 (0.70 V). We have detected three plausible catalytic active sites shown in Figure 7A (labelled as active sites 1–3) where the key *OOH intermediate could form. The optimized geometries for the three *OOH intermediates are shown in Figure 7B. Figure 7C shows the computed free energy profiles of the 2e$^-$-ORR mediated by these three intermediates using the CHE model. The only intermediate in the 2e$^-$-ORR is the *OOH species (where * refers to the active site in the catalysts surface). The free energy of this intermediate can be calculated as follows:[23]

$$\Delta G_{*OOH} = G_{*OOH} + \frac{3}{2}G_{H_2} - G^* - 2G_{H_2O} \quad (1)$$

By a careful examination of the calculated Bader charges (Figure 7B) and the free energy of the processes (Figure 7C) mediated by the **Amide F-COF** fragment model, we determine that active site 2 yields the most favorable pathway. For this active site, the first step is uphill, and the H_2O_2 release step proceeds with a small activation barrier of 0.05 eV at an electrode potential of

Table 1. Summary of the main electrochemical parameters of Imine F-COF and Amide F-COF.

Electrode	E_{onset} vs SCE [mV]	E_{onset} vs RHE [mV]	j_{lim} [mA cm^{-2}]	Tafel Slope [mV dec^{-1}]	R_p [kΩ]	TOF [s^{-1}]	Electron number	$\eta_{experimental}$ [V]
Imine F-COF/GC	−313	+698	−1.23	70.7	4.36	0.085	2.10	0.062
Amide F-COF/GC	−323	+688	−1.29	69.2	6.64	0.155	2.02	0.072
GC	−333	+678	−1.07	120.2	6.82	–	2.50	0.082

0.70 V, indicating high electrochemical activity for this particular reaction. This value is similar to that of 0.03 eV obtained for **Imine F-COF** in previous literature.[23] The reaction paths resulting from active sites 1 and 3 exhibit much higher activation barrier values (downhill in both cases) of 0.29 and 0.68 eV, respectively, further indicating enhanced selectivity among different active sites.

3. Conclusion

In summary, we have investigated the post-synthetic modification of linkages in a fluorinated COF, transforming it into its amide derivative, which serves as a good ORR electrocatalyst. The impact of this linkage modification was compared to its imine counterpart, resulting in enhanced chemical stability while preserving most of the original properties of the crystalline framework. Our study reveals that the linkage modification induces a change in carbon-site adsorption within the framework, thereby enhancing the selectivity, activity, and stability of the new catalyst. These findings underscore the suitability of the COF platform for developing new catalysts with high activity and long-term operability.

Supporting Information

Supporting Information is available from the Wiley Online Library or from the author.

Acknowledgements

M.J.-D. and E.M.-P contributed equally to this work. This work was financially supported by Research Project TED2021-129886B-C43 granted by MCIN/AEI/10.13039/501100011033 and the European Union NextGeneration EU/ PRTR; and Research Project PID2022-138908NB-C33 granted by MCIN/AEI/10.13039/ 501100011033/ and FEDER A way to make Europe, by the Spanish Ministry of Economy and Competitiveness (PID2020-116728RB-I00, TED2021-129738B-I00, PID2022-142262OA-I00, RED2022-134120-T, PID2020-113142RB-C21, PLEC2021-007906 and TED2021-129416A-I00)), Community of Madrid (REACT-UE NANOCOV-CM, TRANSNANOAVANSENS, S2018/NMT-4349; 2021–5A/BIO-20943 and SI3/PJI/2021-00341). J.I.-M. also acknowledges funding from Comunidad de Madrid (Grants S2018/NMT-4367 and Y2020/NMT-6469). M.J.-D. acknowledge Comunidad de Madrid (CT41/22/PEJ-2021-AI/IND-21294) for the predoctoral contract.

Conflict of Interest

The authors declare no conflict of interest.

Data Availability Statement

The data that support the findings of this study are available from the corresponding author upon reasonable request.

Keywords

amide, COF, electrocatalyst, fluorine, H_2O_2, ORR, post-synthesisD

Received: March 16, 2024
Revised: May 14, 2024
Published online:

[1] M. Winter, R. J. Brodd, *Chem. Rev.* **2004**, *104*, 4245.
[2] A. J. Bard, *J. Am. Chem. Soc.* **2010**, *132*, 7559.
[3] H. A. Gasteiger, N. M. Marković, *Science* **2009**, *324*, 48.
[4] G. M. Whitesides, G. W. Crabtree, *Science* **2007**, *315*, 796.
[5] R. Ma, G. Lin, Y. Zhou, Q. Liu, T. Zhang, G. Shan, M. Yang, J. Wang, *NPJ Comput. Mater.* **2019**, *5*, 78.
[6] Y. Zheng, P. Wang, W.-H. Huang, C.-L. Chen, Y. Jia, S. Dai, T. Li, Y. Zhao, Y. Qiu, G. I. N. Waterhouse, G. Chen, *Nano. Lett.* **2023**, *23*, 1100.
[7] E. Martínez-Periñán, I. Bravo, S. J. Rowley-Neale, E. Lorenzo, C. E. Banks, *Electroanalysis* **2018**, *30*, 436.
[8] Y. S. Jeong, J.-B. Park, H.-G. Jung, J. Kim, X. Luo, J. Lu, L. Curtiss, K. Amine, Y.-K. Sun, B. Scrosati, Y. J. Lee, *Nano. Lett.* **2015**, *15*, 4261.
[9] W. Jiao, C. Chen, W. You, J. Zhang, J. Liu, R. Che, *Small* **2019**, *15*, 1805032.
[10] C. Hu, L. Dai, *Angew. Chem., Int. Ed.* **2016**, *55*, 11736.
[11] L. Yang, J. Shui, L. Du, Y. Shao, J. Liu, L. Dai, Z. Hu, *Adv. Mater.* **2019**, *31*, 1804799.
[12] Y. Xu, P. Cai, K. Chen, Q. Chen, Z. Wen, L. Chen, *Angew. Chem., Int. Ed.* **2023**, *62*, 202215584.
[13] A. P. Côté, A. I. Benin, N. W. Ockwig, M. O'Keeffe, A. J. Matzger, O. M. Yaghi, *Science* **2005**, *310*, 1166.
[14] X. Chen, K. Geng, R. Liu, K. T. Tan, Y. Gong, Z. Li, S. Tao, Q. Jiang, D. Jiang, *Angew. Chem., Int. Ed.* **2020**, *59*, 5050.
[15] K. Geng, T. He, R. Liu, S. Dalapati, K. T. Tan, Z. Li, S. Tao, Y. Gong, Q. Jiang, D. Jiang, *Chem. Rev.* **2020**, *120*, 8814.
[16] L. Zheng, Q. Song, P. Tan, S. Wang, X. Liu, L. Sun, *Small* **2023**, *19*, 2207291.
[17] S. Royuela, J. Almarza, M. J. Mancheño, J. C. Pérez-Flores, E. G. Michel, M. M. Ramos, F. Zamora, P. Ocón, J. L. Segura, *Chem.-Eur. J.* **2019**, *25*, 12394.
[18] F. Wen, X. Wu, X. Li, N. Huang, *Chem.-Eur. J.* **2023**, *29*, 202302399.
[19] L. Zhang, G. Yang, S. Xiao, Q. Tan, Q. Zheng, R. Liang, J. Qiu, *Small* **2021**, *17*, 2102944.
[20] M. Martínez-Fernández, E. Martínez-Periñán, J. I. Martínez, M. Gordo-Lozano, F. Zamora, J. L. Segura, E. Lorenzo, *ACS Sustain. Chem. Eng.* **2023**, *11*, 1763.
[21] J. Li, P. Liu, J. Mao, J. Yan, W. Song, *Nanoscale* **2022**, *14*, 6126.
[22] J. Liu, J. Zhao, C. Li, Y. Liu, D. Li, H. Li, V. Valtchev, S. Qiu, Y. Wang, Q. Fang, *Small* **2024**, *20*, 2305759.
[23] M. Martínez-Fernández, E. Martínez-Periñán, A. de la Peña Ruigómez, J. J. Cabrera-Trujillo, J. A. R. Navarro, F. Aguilar-Galindo, D. Rodríguez-San-Miguel, M. Ramos, R. Vismara, F. Zamora, E. Lorenzo, J. L. Segura, *Angew. Chem., Int. Ed.* **2023**, 62, 202313940.
[24] X. Xu, Y. Gao, Q. Yang, T. Liang, B. Luo, D. Kong, X. Li, L. Zhi, B. Wang, *Nano Today* **2023**, *49*, 101792.
[25] S. An, X. Li, S. Shang, T. Xu, S. Yang, C. Cui, C. Peng, H. Liu, Q. Xu, Z. Jiang, J. Hu, *Angew. Chem., Int. Ed.* **2023**, *62*, 202218742.
[26] J. L. Segura, M. J. Mancheño, F. Zamora, *Chem.-Eur. J.* **2016**, *45*, 5635.
[27] G. Jiang, W. Zou, Z. Ou, W. Zhang, Z. Liang, L. Du, *Chem.-Eur. J.* **2023**, *29*, 202203610.
[28] X. Li, S. Cai, B. Sun, C. Yang, J. Zhang, Y. Liu, *Matter* **2020**, *3*, 1507.
[29] S. Li, C. Xiao, H. Jiang, Y. Li, C. Li, *Sci. Bull.* **2023**, *68*, 25.
[30] H. Ding, A. Mal, C. Wang, *Mater. Chem. Front.* **2020**, *4*, 113.
[31] P. J. Waller, S. J. Lyle, T. M. Osborn Popp, C. S. Diercks, J. A. Reimer, O. M. Yaghi, *J. Am. Chem. Soc.* **2016**, *138*, 15519.
[32] F. Helmich, C. C. Lee, M. M. L. Nieuwenhuizen, J. C. Gielen, P. C. M. Christianen, A. Larsen, G. Fytas, P. E. L. G. Leclère, A. P. H. J. Schenning, E. W. Meijer, *Angew. Chem., Int. Ed.* **2010**, *49*, 3939.

[33] L. Chen, J. Du, W. Zhou, H. Shen, L. Tan, C. Zhou, L. Dong, *Chem. Asian J.* **2020**, *15*, 3421.
[34] W. Wang, D. Huang, W. Zheng, X. Zhao, K. He, H. Pang, Y. Xiang, *Chem. Mater* **2023**, *35*, 7154.
[35] Z.-B. Zhou, X.-H. Han, Q.-Y. Qi, S.-X. Gan, D.-L. Ma, X. Zhao, *J. Am. Chem. Soc.* **2022**, *144*, 1138.
[36] H. Qian, F. Meng, C. Yang, X. Yan, *Angew. Chem., Int. Ed.* **2020**, *59*, 17607.
[37] J. Kang, J. Hang, B. Chen, L. Chen, P. Zhao, Y. Xu, Y. Luo, C. Xia, *ACS Appl. Mater. Interfaces.* **2022**, *14*, 57225.
[38] X. Li, S. Yang, M. Liu, X. Yang, Q. Xu, G. Zeng, Z. Jiang, *Angew. Chem., Int. Ed.* **2023**, *62*, 202304356.
[39] X. Li, J. Qiao, S. W. Chee, H.-S. Xu, X. Zhao, H. S. Choi, W. Yu, S. Y. Quek, U. Mirsaidov, K. P. Loh, *J. Am. Chem. Soc.* **2020**, *142*, 4932.
[40] B. H. Toby, R. B. Von Dreele, *J. Appl. Crystallogr.* **2013**, *46*, 544.
[41] L. Zhang, K. Lee, J. Zhang, *Electrochim. Acta.* **2007**, *52*, 3088.
[42] S. D. Bhoyate, J. Kim, F. M. de Souza, J. Lin, E. Lee, A. Kumar, R. K. Gupta, *Coord. Chem. Rev.* **2023**, *474*, 214854.
[43] A. M. Evans, M. R. Ryder, W. Ji, M. J. Strauss, A. R. Corcos, E. Vitaku, N. C. Flanders, R. P. Bisbey, W. R. Dichtel, *Faraday Discuss.* **2021**, *225*, 226.
[44] X. Li, Y. Fu, Q. An, S. Yang, X. Yang, Q. Xu, G. Zeng, Z. Jiang, *Appl. Catal. B* **2024**, *344*, 123611.